Hindawi Publishing Corporation
International Journal of Photoenergy
Volume 2015, Article ID 689702, 8 pages
http://dx.doi.org/10.1155/2015/689702

Research Article

Characteristics of Boron Decorated TiO_2 Nanoparticles for Dye-Sensitized Solar Cell Photoanode

Ching-Yuan Ho,[1,2] J. K. Lin,[1] and Hong-Wen Wang[2,3]

[1]*Department of Mechanical Engineering, Chung Yuan Christian University, Chung-Li 32023, Taiwan*
[2]*Department of Chemistry, Center for Nanotechnology and Institute of Biomedical Technology, Chung Yuan Christian University CYCU, Chung-Li 32023, Taiwan*
[3]*Department of Chemistry, Chung Yuan Christian University, Chung-Li 32023, Taiwan*

Correspondence should be addressed to Ching-Yuan Ho; cyho@cycu.edu.tw

Received 16 May 2015; Accepted 5 August 2015

Academic Editor: Mohammad Muneer

Different boron weight percents on mixed-phase (anatase and rutile) TiO_2 nanoparticles were synthesized to investigate structure morphology, defect states, luminescence properties, and energy conversion. The measured results indicate that boron doping of TiO_2 both increases the crystallite size and rutile-phase percent in an anatase matrix. Decreasing the band gap by boron doping can extend the absorption to the visible region, while undoped TiO_2 exhibits high UV absorption. Oxygen vacancy defects generated by boron ions reduce Ti^{+4} and affect electron transport in dye-sensitized solar cells. Excess electrons originating from the oxygen vacancies of doped TiO_2 downward shift in the conduction band edge and prompt the transfer of photoelectrons from the conduction band of the rutile phase to the lower energy anatase trapping sites; they then separate charges to enhance the photocurrent and J_{sc}. Although the resistance of the electron recombination (R_k) between doped TiO_2 photoanode and the electrolyte for the doped TiO_2 sample is lower, a longer electron lifetime (τ) of 19.7 ms with a higher electron density (n_s) of 2.1×10^{18} cm^{-3} contributes to high solar conversion efficiency.

1. Introduction

Because of the unusual weather induced by enormous carbon dioxide emissions and undisciplined energy utilization, environmental issues have gradually emerged as an important topic. Recently, highly efficient energy conversion products, which are an attempt to eliminate air pollution and to improve environmental qualities, have attracted much attention as replacements for traditional energy utilization devices. Titanium dioxide (TiO_2) is the most promising semiconductor because of its long-term stability, nontoxicity, and low cost; thus, TiO_2 is widely used in various fields, such as dye-sensitized solar cells (DSSCs), removal of organic and inorganic pollutants, and photocatalytic splitting of water for green-energy hydrogen production [1–3]. Among these applications, dye-sensitized solar cells (DSSCs) are advantageous in terms of both technology and the economy because they are low in cost, as compared to inorganic photovoltaic (PV) devices, have higher energy conversion efficiency, and are simple to fabricate. Since 1991, when O'Regan and Grätzel announced the operating principle of a DSSC [4], many studies have extensively focused on the enhanced light collection ability and conductivity of electrons in photoanodes and charge transport behaviors. Unwanted factors reduce DSSC efficiency, including electrons scavenged from photoanodes and the recombination of back electrons with oxidized redox species I^{3-} [5, 6]. The photoexcited capability of oxidized dye molecules has also been studied in order to realize the carrier transport mechanism [7–9]. Recently, many efforts have focused on creating novel structures to enhance PV performance, and the working mechanism of the DSSC system has been gradually realized. Particularly, TiO_2 photoanodes, including core-shell nanowire structures [10, 11], surface treatments and synergistic, mixed-phase TiO_2, and hybrid structures [12–14], which provide a feasible synthesis and a simple method, have been widely utilized to

enhance DSSC efficiency. On the other hand, decorated TiO_2 photoanode technologies have emerged to improve DSSC performance by means of metal/nonmetal doping [15–17].

Metal doping commonly tailors semiconductor properties by, for example, redistributing defects and trapping levels in the band gap and by changing the conduction band position [18–20]. However, metal-doped TiO_2 is impaired due to its thermal instability and increased electron recombination facilities. Instead of metal doping, nonmetal elements such as nitrogen and carbon doping on TiO_2 can change oxygen vacancies and surface-deficiency-related defects and modify the electronic properties. Oxygen plasma and annealing treatments reduce defect trapping and crystallize TiO_2, which results in lower resistivity and contact resistance on the carrier transport pathway. If the surfaces trapping sites and/or energies of lattice are taken into consideration, the anatase trapping site has been shown to be 0.8 eV lower in energy than that of the conduction band, locating it below the rutile conduction band [21, 22]. The synergistic effect in an adequate mixed-phase TiO_2 between heterogeneous anatase and rutile phases facilitates electron migration from the rutile conduction band to the anatase trapping site due to lower energy of anatase trapping sites below the rutile conduction band [23]. The aforementioned methods to modify photoanode TiO_2 result in increased resistance at the TiO_2 anode-electrolyte interfaces and reduced electron recombination, which improves the open-circuit voltage. Among the nonmetallic elements, boron incorporated into rutile TiO_2 leads to the reduction of Ti^{+4} to Ti^{+3}, which improves photocatalytic activity, because Ti^{+3} acts as a photogenerated electron trap [24]. On the other hand, Gopal et al. reported that boron doping was likely to improve the conductivity of TiO_2 because of the reduced valence of the titanium ion and the concomitant increase in the oxygen vacancy with the formation of excess electrons [25, 26]. Recently, researchers have devoted much effort to investigate various photoanode materials and structures, which were expected to suppress interfacial recombination and to improve the parameters of electron transport for increasing power conversion efficiency. Numerous studies have focused on the enhanced light collection ability and conductivity of electrons in photoanode and charge transport behaviors. Although methods of boron doping TiO_2 nanotubes/nanoparticles structures to tailor the position of the conduction band (CB), which redistribute the defect density and trapping level, have been reported [27], the relationship between carriers transport within conduction bands, energy conversion efficiency, and factors negatively affecting DSSC efficiency has not been verified in detail.

In this paper, the content is divided into three sections: characteristics of boron doping of mixed-phase TiO_2; photovoltaic performance; and pathway of photoelectrons. In the first section, crystallite characteristics and changes in the mixed phase associated with various boron doping samples are analyzed by light absorption, luminescence, and defect states. The photovoltaic performances of assembled DSSC devices using various doping TiO_2 photoanodes are verified in the second section. In the third section, we analyze the pathway of photoexcited electrons and correlate the available parameters of electron transport with various boron doping of TiO_2 (B-TiO_2) photoanode on DSSC devices. Under various boron doping conditions on TiO_2, the electrochemical impedance spectrum (EIS) is measured by stressing the open-circuit voltage (V_{oc}) to determine the related parameters, such as electron lifetime (τ), electron density (n_s) in CB, and interfacial resistance (R_k) between TiO_2 and the electrolytes. The obtained PV characteristics relating to the photoanode properties are analyzed in terms of EIS results, deficiencies in photoanodes, and incident photon-to-current conversion efficiency (IPCE).

2. Experimental Details

2.1. Preparation of TiO_2 Electrodes. Prior to the fabrication of the B-TiO_2 nanoparticles, the fluorine-doped tin oxide (FTO) glass substrates were cleaned by the same volume ratio of acetone and isopropyl alcohol mixture in an ultrasonic water bath for 30 min. To prepare B-TiO_2 photoanodes, first, boric acid (H_3BO_3) was added into 50 mL of distilled water under stirring at room temperature to obtain various concentrations of boric acid solution. Subsequently, 1 g of TiO_2 nanoparticles was added dropwise to 20 mL of boric acid mixed solution and the resulting solution was then put into oven in air at 200°C for 36 hours to vaporize water and obtained B-TiO_2 powder. TiO_2 colloidal solution was prepared by adding 0.5 mL of ethanol and distilled water (v/v = 1/1) mixture solution to 0.5 g of B-TiO_2 powder and 0.15 g of polyethylene glycol (PEG). The mixture was ultrasonicated for 3 h to form the TiO_2 colloidal solution. The TiO_2 photoanodes were prepared layer-by-layer coating of the as-synthesized TiO_2 colloidal solution on the fluorine-doped SnO_2 (FTO) glasses using a glass rod. The purpose of PEG is used to generate mesoporous TiO_2 photoelectrode for future dye adhesion. All as-prepared TiO_2 nanoparticles were calcined at 450°C for 30 min in air atmosphere to form microstructure and the thickness was about 14 μm.

2.2. Fabrication of the DSSC Devices. Synthesis of undoped and B-TiO_2 nanoparticles were pasted on conducting FTO glass substrate with an active area of 0.5 cm × 0.5 cm and then immersed in a 3.0×10^{-3} M solution of the ruthenium based dye $[RuL_2(NCS)_2]TBA_2$ for overnight, where Ru is ruthenium, L stands for 2,2′-bipyridyl-4,4′-dicarboxylic acid, NCS represents isothiocyanate, and TBA is tetra-n-butylammonium (N719 dye, Everlight Chemical, Taiwan). The specimens were washed with ethanol after immersion in N719 dye solution. A thin Pt sputtered on an FTO glass was used as the counter electrode. The iodide/tri-iodide (I^-/I_3^-) electrolyte (lodolyte R-150) was cast onto the dye absorbed TiO_2 electrodes. The TiO_2 electrodes and the Pt coated electrodes were clamped together to assemble the DSSC devices.

2.3. Characteristics Measurement. In order to study the physical and electrical properties, the decorated boron of TiO_2 nanoparticles was characterized. The field emission scanning electron microscope (FESEM, JEOL 7600F) with energy dispersive X-ray spectroscopy (EDS) was used to determine the surface morphology, thickness of the films, and boron

weight percentage in TiO_2. The crystalline phases of the obtained titania electrodes were analyzed by Raman spectra and X-ray diffractometer with a Cu-Kα line target ($\lambda = 1.54$ Å) and Ni filter at a scanning rate of 2°/min from $2\theta = 20°$ to 80°. Photoluminescence spectroscopy (PL) was used to observe the change of defect states and band characteristics with increasing boron doping. The photovoltaic characteristics of DSSC devices were measured from an illuminated area of 0.5 cm × 0.5 cm under standard AM 1.5 sunlight illumination (XES-151S, San-Ei, Japan) with 100 mW/cm^2 light source from the solar simulator and Keithley 2420 SourceMeter. The EIS results was obtained using electrochemical analyzer (CHI 6173b, CH Instruments Co., USA) in the range from 0.01 Hz to 100 kHz within the alternating current amplitude of 10 mV open-circuit voltage (V_{oc}) under the condition of zero electric current. The IPCE was measured within the range of 350–800 nm wavelengths using an IPCE system (Enlitech, Taiwan) that was specifically designed for DSSCs.

3. Results and Discussion

The properties of boron-doped TiO_2 nanoparticles are discussed and then analyze the performance of the assembled DSSC devices using various boron-doped TiO_2 nanoparticles as photoanode.

3.1. TiO_2 Nanoparticle Properties. Figures 1(a)~1(c) show the top view and cross-sectional SEM images of undoped and doped TiO_2 nanoparticles. The weight percentage of each synthesized doped TiO_2 was measured by EDS (not shown here), and the values of 8%, 5.8%, and 3.5% were designated as BT-8, BT-5, and BT-3, respectively. It is found that the boron content confirmed by EDS increases with the boric acid concentration. As shown in Figure 1(a), undoped TiO_2 nanoparticle (assigned to BT-0) with an approximate spherical shape has an average particle size of approximately 20–30 nm; BT-8, as shown in Figure 1(b), has a slightly smaller diameter but more aggregation as compared with the undoped TiO_2 sample. Figure 1(c) shows that the TiO_2 nanoparticles are well pasted onto FTO glass substrate with no peeling between interfaces. Moreover, mesoporous TiO_2 nanoparticles synthesized by PEG addition are desirable for future dye adhesion to enhance photogenerated electrons and improvement to light conversion efficiency in DSSCs. Figure 1(d) schematically depicts the assembled DSSC structure, electron transport, and recombination pathways. Figure 2 shows the XRD spectra of all doping TiO_2 samples after annealing at 450°C for 30 minutes; a major anatase phase incorporated with a rutile phase is found. The peak positions consist of anatase phase and rutile phase with preferential orientations of (101) plane and (110), respectively [28]. The peak intensities of plane (101) increase with the decorated boron content; meanwhile, plane (110) is observed. According to the following equation, the compositions change between the anatase and the rutile phases is determined from the XRD results:

$$W_R = \frac{A_R}{0.884 \times A_A + A_R}, \quad (1)$$

where A_A, A_R, and W_R represent the integrated intensity of the anatase (101) peak, the integrated intensity of the rutile (110) peak, and the rutile weight percentage, respectively. The weight percentages of rutile crystallite in all samples (BT-0 to BT-8) increase with the boron concentration and are calculated to be 9.0, 9.5, 10, and 12 wt%, respectively. Due to the fact that the crystal size is inversely proportional to full width at half maximum (FWHM) by the Scherrer equation, the crystal size of boron doping TiO_2 increases with boron concentration as shown in Figure 2. For boron doping on TiO_2, interstitial boron contributes three valence electrons to 3D states of the titanium ion, and then Ti^{+4} ions are reduced to Ti^{+3} following the formation of an oxygen vacancy ($V_O{}^{+2}$) with excess free electrons

$$B + 3Ti^{+4} \longrightarrow B^{+3} + 3Ti^{+3} + V_O{}^{+2} + 2e^- \quad (2)$$

Thus, increased boron doping on TiO_2 nanoparticles result in increased oxygen vacancies and free electron formations [29]. The phase transformation between anatase and rutile is dominated by boron into anatase TiO_2 causing a reduction of Ti^{+4} to Ti^{+3}, and then free electrons accumulated at conduction band and facilitated charge separation by band bending [24]. Generally, PL spectra of anatase TiO_2 materials consist of three kinds of physical origins: oxygen vacancies, self-trapped excitons, and surface states. Figure 3 illustrates the PL spectra of all samples prepared with various boron decorations on TiO_2. It can be seen that the PL intensities increase by boron doping concentration, with the high peak intensity for decorated samples, indicating the presence of defects states within the mixed phase of the anatase-rutile structure. The highest PL intensity of BT-8 is due to the self-trapped excitons combined with the defect states stemming from the oxygen vacancies and surface-related defects [30–33]. The shallow traps identified with oxygen vacancies at 402 nm have been reported [30, 31]; the observed 460 nm and 532 nm bands relating to the trapping levels of 0.51 eV and 0.8 eV below the conduction band could be assigned to the defect level due to the oxygen vacancies and surface defects, respectively [32, 33]. The inset of Figure 3, which is extracted from Gauss distribution of Figure 3, shows that an additional PL peaks appear at around 395–405 nm, attributed to the transient of shallow donor level in forbidden gap which corresponds to the oxygen vacancy-related defect level. A visible emission at 485 nm presents for all prepared samples and could be attributed to the charge transfer from Ti^{+3} to complex ($TiO_6{}^{-8}$) complex, indicating that the band originated from the intrinsic states rather than the surface state. Thus, the 485 nm band could be assigned to self-trapped excitons localized on a TiO_6 octahedral. In this experiment, the composition change of the mixed phase on anatase-rutile is attributed to boron decoration. These mixed-phase structures create the shallow traps and defect levels in the depth of the band gap and exhibit a multiplicity of photoluminescence characteristics. Raman scattering is an additional method to verify crystallite size and phase transformation. Typically, there are five active modes contained in anatase TiO_2, Eg (144 cm^{-1}), Eg (196 cm^{-1}), B1g (396 cm^{-1}), A1g + B1g (518 cm^{-1}), and Eg

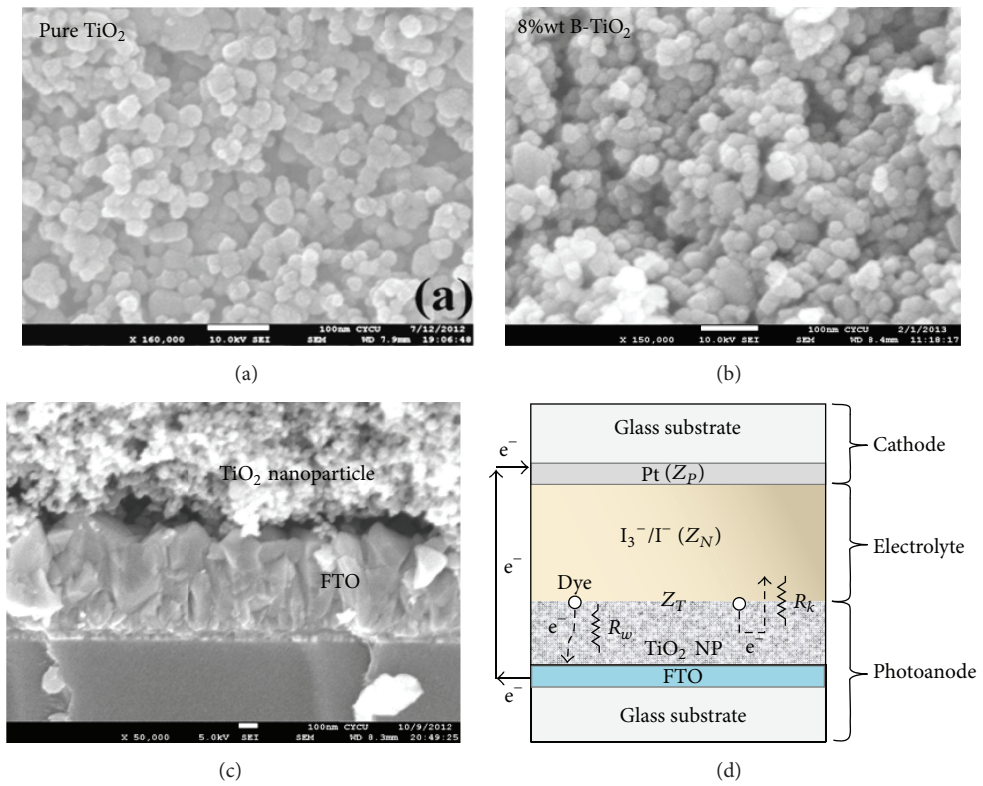

FIGURE 1: SEM images of the TiO_2 nanoparticles: (a) BT-0, (b) BT-8, (c) interface between TiO_2 nanoparticle and FTO substrate, and (d) schematic drawing of assembling DSSC structure, electron transport, and recombination pathways.

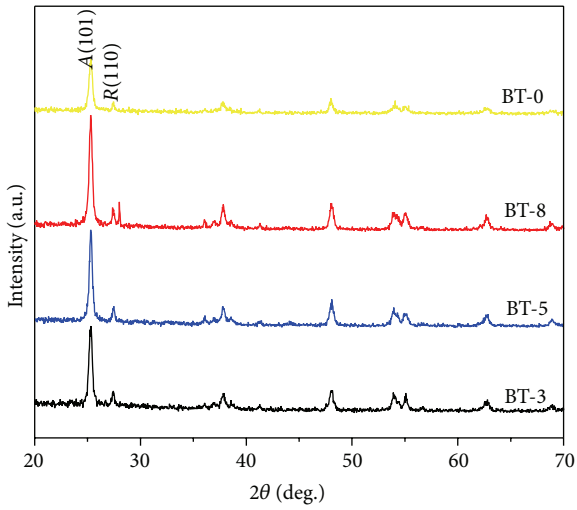

FIGURE 2: XRD patterns of undoped and boron doping TiO_2 nanoparticles including 8%, 5%, and 3.5% weight percentage assigned as BT-0, BT-8, BT-5, and BT-3, respectively.

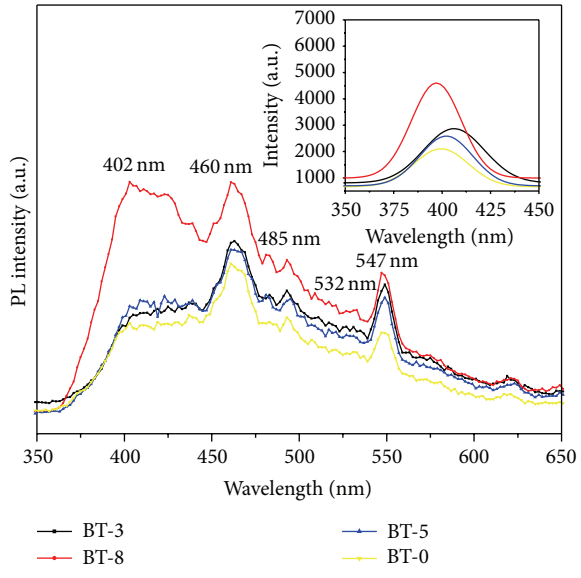

FIGURE 3: Photoluminescence spectra of undoped and doped samples.

(639 cm^{-1}), and one active mode, Eg (240 cm^{-1}), in rutile TiO_2. Figure 4 shows the Raman spectra of boron-decorated TiO_2 samples ranging from 100 cm^{-1} to 1000 cm^{-1}. Based on the phonon confinement model formed by the Heisenberg uncertainty principle, a relationship exists between crystallite size and phonon momentum distribution. As the particle size shrinks, the phonons are confined increasingly within the particles and phonon momentum distribution increases [34, 35]. Figure 4 indicates that the FWHM of TiO_2 is not obviously different by boron concentration which means crystal size is similar between various boron concentrations.

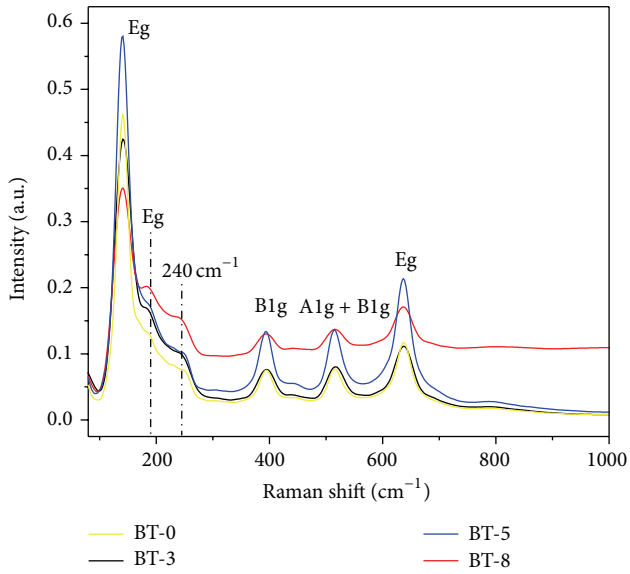

Figure 4: Raman spectra of boron doping samples.

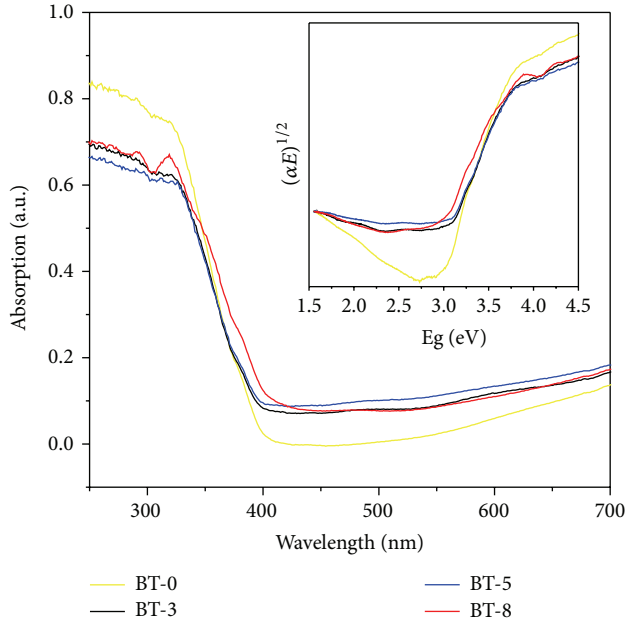

Figure 5: UV-vis spectra with different doping conditions.

Although it is controversial with XRD results, another mode of frequency at 240 cm^{-1}, which is a unique feature of rutile TiO_2 nanocrystals, is observed. It is evident that the rutile composition qualitatively increases with peak intensity by the boron decoration, as confirmed by the XRD results. Figure 5 illustrates the UV-visible absorption spectra in the wavelengths 200–800 nm. It is obvious that the absorption edge slightly tends to longer wavelength for all doped samples (called a red shift), while a higher UV absorption region is found on undoped samples. Based on the Tauc equation, by plotting the curve of $(\alpha E)^{1/2}$ versus E (α is the absorption coefficient and E is the light energy) shown in the inset of Figure 5, the optical band gap is calculated to be 3.1 eV for undoped TiO_2 and 2.8–2.92 eV for B-TiO_2. This illustrates that the decrease in the optical band gap could be attributed to the boron decoration and that it also improves energy conversion efficiency in visible region.

3.2. Photovoltaic Performance of DSSC. As shown in Figure 1(d), decorated TiO_2 that acted as photoanode on DSSC device was investigated. Figure 6 shows the photocurrent density-voltage characteristics of the DSSC with various boron doping of TiO_2 photoanodes under a simulated solar light of 100 mW/cm^2. Among them, BT-8 has an obvious increase in J_{sc} and the highest energy conversion efficiency (η) of 4.6% is 21% higher than that of BT-0 sample. Because the Fermi energy position of the anatase trapping site is below the rutile conduction band, in an adequate doping concentration in mixed-phase TiO_2, the excess electrons accumulate and there is a downward shift in the conduction band edge at the anatase-rutile grain boundary. The downward shift in the conduction band self-generates a built-in potential and facilitates electrons injected from the rutile phase into the lower energy level of the anatase trapping site, leading to a charge separation. The open-circuit

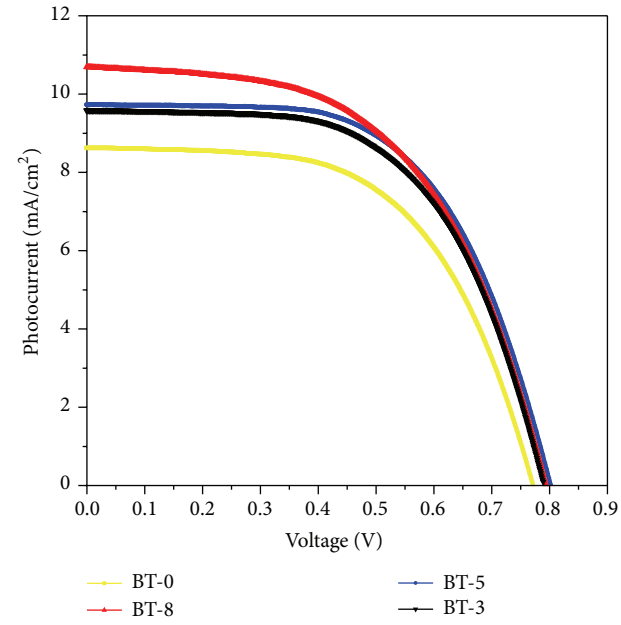

Figure 6: J-V plots measured by various TiO_2 photoanodes of DSSC devices.

voltage ($V_{oc} = I \times R_k$) values are not obviously different between experimental samples which will be explained by following EIS section. The energy diagram shown in Figure 7 depicts the pathway of excited photoelectrons injected from the dye to the rutile conduction band, anatase trapped level in the band gap and arrive photoanode surface.

3.3. Parameters of Electron Transport Determined by EIS. Regarding the assembling DSSC device, the pathway of the carrier transport, the conductivity of TiO_2 nanoparticles, the

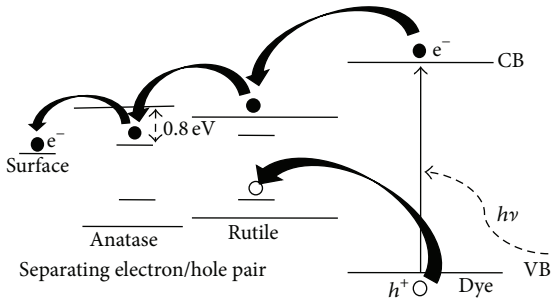

FIGURE 7: Energy diagram and carrier transportation of mixed-phase TiO_2 nanoparticles.

behavior of the photoelectron injection, and back-electron recombination correlated with PV parameters are now discussed in terms of the EIS analysis.

Based on the impedance equation of recombination in TiO_2-electrolyte-dye and the carrier transport pathway proposed by Bisquert and Adachi et al., three types of impedance and electron pathways are summarized in the DSSC system [36, 37]. The total impedance (Z_S) is given by the sum of the impedance at the Pt electrode/electrolyte interface (Z_P), the impedance of tri-iodide diffusion in the electrolyte (Z_N), and the sum of the impedance of diffusion and recombination in TiO_2 photoanode (Z_T). The impedance of Z_T consists of R_k and R_ω, which represent the charge-transfer resistance relating to the electron recombination in electrolytes and the electron transport resistance in TiO_2 photoanodes, respectively. All electron transport parameters on the DSSCs, including the charge-transfer resistance relating to electron recombination (R_k), electron lifetime (τ), and electron density (n_s) on CB, were evaluated using EIS measurement. Figure 8(a) shows the typical experimental spectra of the Nyquist plot. Peaks contained three arcs ω_1, ω_2, and ω_3 which are assigned to the charge transport within the Pt counter electrode/electrolyte interface (Z_P), the TiO_2 photoanode-electrolyte-dye system (Z_T), and the diffusion of tri-iodide ions within the electrolyte (Z_N), respectively. The R_k value at the TiO_2-electrolyte interface relating to the electron recombination is determined by the diameter of central arc ω_2. Moreover, at a steady state, the electron density n_s in the conduction band of TiO_2 photoanodes could be calculated as follows:

$$n_s = \frac{K_B T}{q^2 \times A \times \text{Con}} \quad \text{Con} = L \times K_{\text{eff}} \times R_k, \tag{3}$$

where L, K_{eff}, q^2, A, n_s, K_B, and T represent the TiO_2 photoanode thickness, the peak frequency of the central arc ω_2 (near 10), the charge of an electron, the electrode area, the electron density in the conduction band, the Boltzmann constant, and the absolute temperature, respectively. The lifetime (τ) of photoinjected electrons within the TiO_2 photoanode can be expressed as $1/2\pi f$, where the highest peak frequency f is provided via the Bode phase plot (shown in Figure 8(b)). All photovoltaic parameters and EIS parameters are shown in Table 1. The R_k values for the B-TiO_2 samples relating

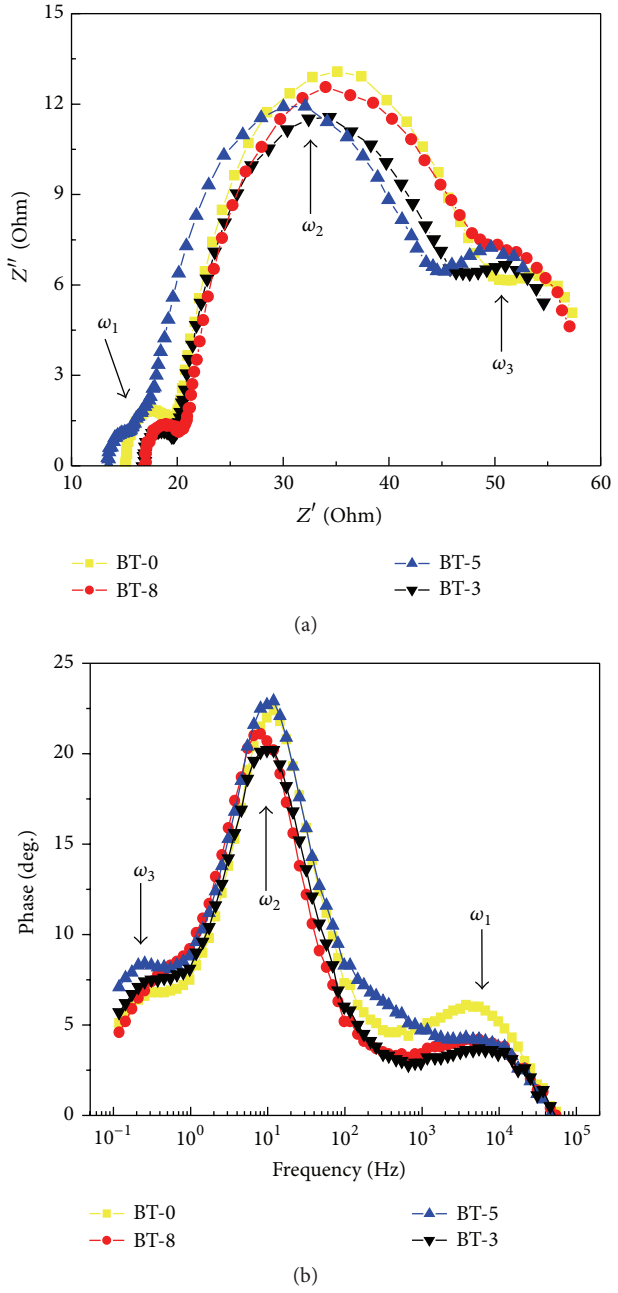

FIGURE 8: DSSC contains different B-TiO_2. (a) Nyquist plot shows typical three arcs corresponding to specific resistance in photoanode-electrolyte-dye system, (b) Bode plot related to peak frequency represents electron lifetime.

to the back-electron recombination at the TiO_2 photoanode/electrolyte interface, which is proportional to the V_{oc}, are slightly lower than those for the undoped TiO_2 samples; this is attributed to the high oxygen vacancy contained in boron doping of TiO_2 photoanodes, which increase the possibility for electron recombination. On the other hand, both a longer electron lifetime of 19.7 ms and a higher electron concentration of 2.1×10^{18} cm^{-3} on BT-8 sample facilitate electron transport on conduction band and increased energy

Table 1: Photovoltaic and EIS parameters by various TiO_2 photoanodes of DSSC devices.

Photovoltaic and EIS parameter of DSSC with various anodes							
Anode	J_{sc} (mA/cm^2)	V_{oc} (V)	FF	η (%)	R_k (Ω)	τ_{eff} (ms)	n_s (cm^{-3})
BT-0	8.62	0.77	0.6	3.83	29.6	13.3	1.3×10^{18}
BT-8	10.69	0.79	0.5	4.61	27.1	19.7	2.1×10^{18}
BT-5	9.72	0.80	0.6	4.62	27.5	15.2	1.6×10^{18}
BT-3	9.58	0.79	0.6	4.42	26.4	16.4	1.8×10^{18}

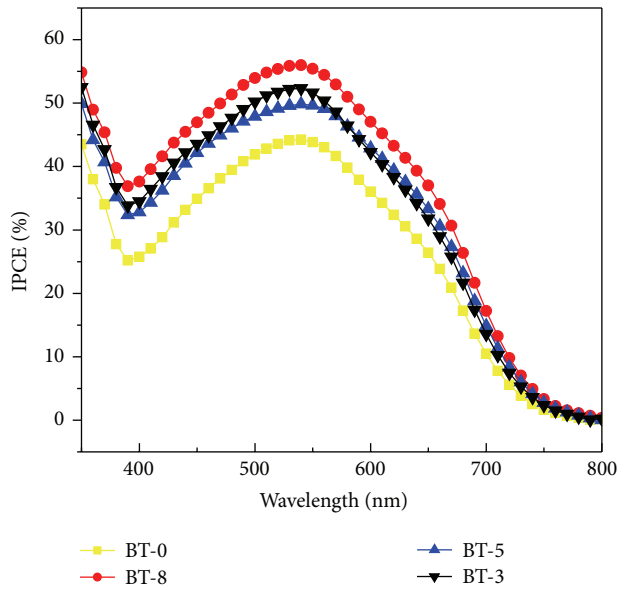

Figure 9: IPCE spectra of the dye-sensitized solar cell using mixed phase of boron-doped TiO_2 as photoanode.

conversion efficiency because the rich oxygen vacancies in B-TiO_2 also improve the conductivity of TiO_2 photoanodes and J_{sc}. Therefore, the lower R_k values in boron doping samples could obtain similar V_{oc} result compared with BT-0 sample and thus the V_{oc} values are compensated due to higher current density. The photocurrent of DSSC based on different boron doping conditions is also identified by the IPCE measurement. During photoexcitation, the photogenerated electrons are injected from photoexcited N719 dye molecules to the rutile conduction band and then transfer to the anatase conduction band. Figure 9 shows an improvement of 25% in the photocurrent in BT-8 compared with BT-0. This indicates that the excess electrons originated from n-type boron-doped TiO_2 and downward shift in the conduction band edge at the anatase-rutile grain boundary; thus, the charge separation of photoexcited electrons enhances the photocurrent. In this study, BT-8 sample has high possibility of electrons recombination, but it also possesses longer electron lifetime and much electron concentration; thus, it has the highest energy conversion efficiency.

4. Conclusions

Boron doping with mixed-phase TiO_2 photoanodes relating to photovoltaic performance and electrochemical impedance spectrum on DSSC was investigated in this study. Boron doping in TiO_2 nanoparticles changes the composition of anatase-rutile. Rich oxygen vacancies and excess electrons within TiO_2 nanoparticles also facilitate the fast electrons injected from the rutile conduction band into the lower energy at the anatase trapping site, finally prompting the charge separation and enhancing the photocurrent and J_{sc}. However, oxygen vacancies also reduce the resistance of the electron recombination between photoanodes/electrolytes. On the other hand, the electron lifetime and electron density in oxygen-vacancy-rich B-TiO_2 specimens conquer the drawback of electron recombination and improve energy conversion efficiency.

Conflict of Interests

The authors declare that there is no conflict of interests regarding the publication of this paper.

References

[1] K. Yang, Y. Dai, and B. Huang, "Origin of the photoactivity in boron-doped anatase and rutile TiO_2 calculated from first principles," *Physical Review B*, vol. 76, Article ID 195201, 2007.

[2] X. Wang, K. L. Yang, Z. H. Jiang, and R. Q. Fan, "Preparation of TiN_xO_{2-x} photoelectrodes with NH_3 under controllable middle pressures for dye-sensitized solar cells," *European Journal of Inorganic Chemistry*, vol. 2009, no. 23, pp. 3481–3487, 2009.

[3] N. Bahadur, K. Jain, A. K. Srivastavaa, R. Govinda, D. Haranatha, and M. S. Dulat, "Effect of nominal doping of Ag and Ni on the crystalline structure and photo-catalytic properties of mesoporous titania," *Materials Chemistry and Physics*, vol. 124, no. 1, pp. 600–608, 2010.

[4] B. O'Regan and M. Grätzel, "A low-cost, high-efficiency solar cell based on dye-sensitized colloidal TiO_2 films," *Nature*, vol. 353, no. 6346, pp. 737–740, 1991.

[5] S. H. Szczepankiewicz, A. J. Colussi, and M. R. Hoffmann, "Infrared spectra of photoinduced species on hydroxylated titania surfaces," *Journal of Physical Chemistry B*, vol. 104, no. 42, pp. 9842–9850, 2000.

[6] W. Göpel, G. Rocker, and R. Feierabend, "Intrinsic defects of TiO2(110): interaction with chemisorbed O2, H2, CO, and CO2," *Physical Review B*, vol. 28, no. 6, article 3427, 1983.

[7] X. Zhang, F. Liu, Q.-L. Huang, G. Zhou, and Z.-S. Wang, "Dye-sensitized W-doped TiO_2 solar cells with a tunable conduction band and suppressed charge recombination," *Journal of Physical Chemistry C*, vol. 115, no. 25, pp. 12665–12671, 2011.

[8] A. K. Chandiran, F. Sauvage, M. Casas-Cabanas, P. Comte, S. M. Zakeeruddin, and M. Grätzel, "Doping a TiO_2 photoanode with Nb^{5+} to enhance transparency and charge collection efficiency in dye-sensitized solar cells," *The Journal of Physical Chemistry C*, vol. 114, no. 37, pp. 15849–15856, 2010.

[9] X. Lü, X. Mou, J. Wu et al., "Improved-performance Dye-Sensitized solar cells using Nb-Doped TiO_2 electrodes: efficient electron Injection and transfer," *Advanced Functional Materials*, vol. 20, no. 3, pp. 509–515, 2010.

[10] C. Rochford, Z.-Z. Li, J. Baca, J. Liu, J. Li, and J. Wu, "The effect of annealing on the photoconductivity of carbon nanofiber/TiO_2 core-shell nanowires for use in dye-sensitized solar cells," *Applied Physics Letters*, vol. 97, no. 4, Article ID 043102, 2010.

[11] Z. Li, C. Rochford, F. J. Baca, J. Liu, J. Li, and J. Wu, "Investigation into photoconductivity in single CNF/TiO_2-dye core-shell nanowire devices," *Nanoscale Research Letters*, vol. 5, no. 9, pp. 1480–1486, 2010.

[12] J. Wu, G. R. Chen, C. C. Lu, W. T. Wu, and J. S. Chen, "Performance and electron transport properties of TiO_2 nanocomposite dye-sensitized solar cells," *Nanotechnology*, vol. 19, no. 10, Article ID 105702, 2008.

[13] Y. Alivov and Z. Y. Fan, "Efficiency of dye sensitized solar cells based on TiO2 nanotubes filled with nanoparticles," *Applied Physics Letters*, vol. 95, no. 6, Article ID 063504, 2009.

[14] B. Tan and Y. Wu, "Dye-sensitized solar cells based on anatase TiO_2 nanoparticle/nanowire composites," *The Journal of Physical Chemistry B*, vol. 110, no. 32, pp. 15932–15938, 2006.

[15] Y. Zhang, L. Wang, B. Liu et al., "Synthesis of Zn-doped TiO_2 microspheres with enhanced photovoltaic performance and application for dye-sensitized solar cells," *Electrochimica Acta*, vol. 56, no. 18, pp. 6517–6523, 2011.

[16] N. Tsvetkov, L. Larina, O. Shevaleevskiy, and B. T. Ahn, "Effect of Nb doping of TiO_2 electrode on charge transport in dye-sensitized solar cells," *Journal of the Electrochemical Society*, vol. 158, no. 11, pp. B1281–B1285, 2011.

[17] X. Zhang, S. T. Wang, and Z. Wang, "Effect of metal-doping in TiO_2 on fill factor of dye-sensitized solar cells," *Applied Physics Letters*, vol. 99, no. 11, Article ID 113503, 2011.

[18] S. Gubbala, V. Chakrapani, V. Kumar, and M. K. Sunkara, "Band-edge engineered hybrid structures for dye-sensitized solar cells based on SnO_2 nanowires," *Advanced Functional Materials*, vol. 18, no. 16, pp. 2411–2418, 2008.

[19] X. Chen and S. S. Mao, "Titanium dioxide nanomaterials: synthesis, properties, modifications and applications," *Chemical Reviews*, vol. 107, no. 7, pp. 2891–2959, 2007.

[20] H. Tian, L. Hu, C. Zhang et al., "Retarded charge recombination in dye-sensitized nitrogen-doped tio 2 solar cells," *The Journal of Physical Chemistry C*, vol. 114, no. 3, pp. 1627–1632, 2010.

[21] D. C. Hurum, A. G. Agrios, and K. A. Gray, "Explaining the enhanced photocatalytic activity of degussa P25 mixed-phase TiO_2 using EPR," *The Journal of Physical Chemistry B*, vol. 107, no. 19, pp. 4545–4549, 2003.

[22] S. Leytner and J. T. Hupp, "Evaluation of the energetics of electron trap states at the nanocrystalline titanium dioxide/aqueous solution interface via time-resolved photoacoustic spectroscopy," *Chemical Physics Letters*, vol. 330, no. 3-4, pp. 231–236, 2000.

[23] G. Li, C. P. Richter, R. L. Milot et al., "Synergistic effect between anatase and rutile TiO_2 nanoparticles in dye-sensitized solar cells," *Dalton Transactions*, no. 45, pp. 10078–10085, 2009.

[24] I. E. Grey, C. Li, C. M. MacRae, and L. A. Bursill, "Boron incorporation into rutile. Phase equilibria and structure considerations," *Journal of Solid State Chemistry*, vol. 127, no. 2, pp. 240–247, 1996.

[25] N. O. Gopal, H.-H. Lo, and S.-C. Ke, "Chemical state and environment of boron dopant in B,N-codoped anatase TiO2 nanoparticles: an avenue for probing diamagnetic dopants in TiO_2 by electron paramagnetic resonance spectroscopy," *Journal of the American Chemical Society*, vol. 130, no. 9, pp. 2760–2761, 2008.

[26] E. Finazzi, C. D. Valentin, and G. Pacchioni, "Boron-doped anatase TiO_2: pure and hybrid DFT calculations," *Journal of Physical Chemistry C*, vol. 113, no. 1, pp. 220–228, 2009.

[27] A. Subramanian and H.-W. Wang, "Effects of boron doping in TiO_2 nanotubes and the performance of dye-sensitized solar cells," *Applied Surface Science*, vol. 258, no. 17, pp. 6479–6484, 2012.

[28] R. Restori, D. Schwarzenbach, and J. R. Schneider, "Charge density in rutile, TiO_2," *Acta Crystallographica Section B: Structural Science*, vol. 43, pp. 251–257, 1987.

[29] H. J. Tian, L. H. Hu, C. N. Zhang et al., "Enhanced photovoltaic performance of dye-sensitized solar cells using a highly crystallized mesoporous TiO_2 electrode modified by boron doping," *Journal of Materials Chemistry*, vol. 21, no. 3, pp. 863–868, 2011.

[30] L. V. Saraf, S. I. Patil, S. B. Ogale, S. R. Sainkar, and S. T. Kshirsager, "Synthesis of nanophase TiO_2 by ion beam sputtering and cold condensation technique," *International Journal of Modern Physics B*, vol. 12, no. 25, pp. 2635–2647, 1998.

[31] N. Serpone, D. Lawless, and R. Khairutdinov, "Size effects on the photophysical properties of colloidal anatase TiO_2 particles: size quantization or direct transitions in this indirect semiconductor?" *The Journal of Physical Chemistry*, vol. 99, no. 45, pp. 16646–16654, 1995.

[32] H. Tang, H. Berger, P. E. Schmid, F. Lévy, and G. Burri, "Photoluminescence in TiO_2 anatase single crystals," *Solid State Communications*, vol. 87, no. 9, pp. 847–850, 1993.

[33] L. Forss and M. Schubnell, "Temperature dependence of the luminescence of TiO2 powder," *Applied Physics B*, vol. 56, no. 6, pp. 363–366, 1993.

[34] T. Ohsaka, F. Izumi, and Y. Fujiki, "Raman spectrum of anatase, TiO_2," *Journal of Raman Spectroscopy*, vol. 7, no. 6, pp. 321–324, 1978.

[35] D. Bersani, P. P. Lottici, and X.-Z. Ding, "Phonon confinement effects in the Raman scattering by TiO_2 nanocrystals," *Applied Physics Letters*, vol. 72, no. 1, pp. 73–75, 1998.

[36] M. Adachi, M. Sakamoto, J. Jiu, Y. Ogata, and S. Isoda, "Determination of parameters of electron transport in dye-sensitized solar cells using electrochemical impedance spectroscopy," *Journal of Physical Chemistry B*, vol. 110, no. 28, pp. 13872–13880, 2006.

[37] J. Bisquert, "Theory of the impedance of electron diffusion and recombination in a thin layer," *Journal of Physical Chemistry B*, vol. 106, no. 2, pp. 325–333, 2002.